Ulrich Schwarz*, Rodrigo Castillo, Julia M. Hübner, Aron Wosylus, Yurii Prots, Matej Bobnar and Yuri Grin

The untypical high-pressure Zintl phase $SrGe_6$

https://doi.org/10.1515/znb-2019-0197
Received November 21, 2019; accepted November 28, 2019

Abstract: The binary strontium germanide $SrGe_6$ was synthesized at high-pressure high-temperature conditions of approximately 10 GPa and typically 1400 K before quenching to ambient conditions. At ambient pressure, $SrGe_6$ decomposes in a monotropic fashion at $T = 680(10)$ K into $SrGe_2$ and Ge, indicating its metastable character. Single-crystal X-ray diffraction data indicate that the compound $SrGe_6$ adopts a new monoclinic structure type comprising a unique three-dimensional framework of germanium atoms with unusual cages hosting the strontium cations. Quantum chemical analysis of the chemical bonding shows that the framework consists of three- and four- bonded germanium atoms yielding the precise electron count $Sr[(4bGe^0]_4[(3b)Ge^-]_2$ in accordance with the $8-N$ rule and the Zintl concept. Conflicting with that, a pseudo-gap in the electronic density of states appears clearly below the Fermi level, and elaborate bonding analysis reveals additional Sr–Ge interactions in the concave coordination polyhedron of the strontium atoms.

Keywords: germanium; high-pressure synthesis; strontium; Zintl phase.

Dedicated to: Professor Arndt Simon on the occasion of his 80th birthday.

1 Introduction

A number of tetrel-rich atomic arrangements comprise anionic frameworks formed by *p*-block elements. Silicon-rich compounds MSi_6 (M = Ca, Sr, Ba, Eu) [1–5] are characterized by four-bonded network atoms implying an excess of electrons with respect to the 8–*N* rule and the Zintl-Klemm concept. This surplus may be described by the charge balance $M^{2+}[(4b)Si_6^0] \times 2e^-$. Although compositions with a significantly reduced excess of electrons may be realized by chemical substitution [6] or vacancy formation [7–9], e.g. in the modulated silicide $CeSi_{1.82}$ [10], the development of defects is more typical for polyanions of germanium or tin. In these compounds, the electron excess of the framework is reduced (or even completely compensated) by the formation of defects, which are surrounded by atoms bearing free electron pairs [7–9]. The vacancies are often randomly distributed [7], but a few commensurate superstructures have been reported, e.g. for $Ba_8Ge_{43}\square_3$ [8] and $M_8Sn_{44}\square_2$ (M = Rb, Cs [9]). Similarly, in samples $SrGe_{6-x}$ with $x \approx 0.5$ [7], the $EuGa_2Ge_4$-type crystal structure [11, 12] exhibits a significant number of vacancies in the network. In a first study, the arrangement of these voids has been described by a disorder model involving one randomly half-occupied germanium position [7]. Later, an independent investigation evidenced satellite reflections for composition $x \approx 0.45$ [13], which unveil incommensurate modulation of the vacancy pattern.

In the present concerted experimental and theoretical study, we report on the high-pressure, high-temperature synthesis and the crystal structure of $SrGe_6$ and the solid solution $Sr(Ge_{1-x}Si_x)_6$ ($x = 0.41$). The bonding properties of the binary compound are analyzed by quantum-chemical methods operating in positional space.

2 Experimental

Preparation and sample handling except the high-pressure, high-temperature synthesis was performed in argon-filled glove boxes (MBraun, $H_2O < 0.1$ ppm; $O_2 < 0.1$ ppm) in order to avoid contamination of the product. $SrGe_2$ was prepared as a precursor by arc-melting of strontium-germanium mixtures with an atomic ratio of 1:2.

For the high-pressure synthesis of $SrGe_6$, $SrGe_2$ was mixed with germanium to yield a final ratio Sr:Ge of 1:6. For the quasi-binary phase $Sr(Ge_{1-x}Si_x)_6$, a mixture of composition Sr:Ge:Si = 1:3:3 was prepared. The feed materials were placed in crucibles machined from hexagonal boron nitride. High-pressure, high-temperature experiments were performed in an octrahedral multianvil press with MgO octrahedra of 14 mm edge length [14]. High temperatures were realized by resistive heating of graphite tubes. Pressure and temperature calibration had been performed

***Corresponding author: Ulrich Schwarz,** Max-Planck-Institut für Chemische Physik fester Stoffe, Nöthnitzer Straße 40, 01187 Dresden, Germany, e-mail: schwarz@cpfs.mpg.de
Rodrigo Castillo, Julia M. Hübner, Aron Wosylus, Yurii Prots, Matej Bobnar and Yuri Grin: Max-Planck-Institut für Chemische Physik fester Stoffe, Nöthnitzer Straße 40, 01187 Dresden, Germany

prior to the experiments by *in situ* monitoring of the resistance changes of bismuth [15], and by performing calibration heating runs with a thermocouple, respectively. Samples were subjected to pressures of typically 8(1)–10(1) GPa and 1100(100)–1600(150) K applying annealing times between 30 min and 5 h.

Phase identification was realized by powder X-ray diffraction experiments (Huber image plate Guinier camera G670) employing Cu$K\alpha_1$ radiation, $\lambda = 1.54056$ Å. Single crystal X-ray diffraction data was measured with a Rigaku AFC7 diffractometer operated with Mo$K\alpha$ radiation ($\lambda = 0.71073$ Å) and a Mercury CCD detector. For crystal structure refinement and crystallographic calculations, the program package WinCSD [16] was used.

Differential Scanning Calorimetry (DSC) experiments were performed with closed alumina crucibles in argon atmosphere (Netzsch DSC 404c) at temperatures between 473 and 1223 K. For the observed effects, onset temperatures are given in the text and in the figures.

3 Quantum chemical calculations

Electronic structure calculations and bonding analysis were carried out with the TB-LMTO-ASA [17] program package using the experimentally determined lattice parameters and atomic coordinates (Tables 1 and 2). The Barth-Hedin exchange potential [18] was employed and the radial scalar-relativistic Dirac equation was solved to get the partial waves. Although the calculation within the atomic sphere approximation (ASA) already includes corrections for the neglect of interstitial regions and partial waves of higher order [19], the addition of empty spheres was necessary. The following radii of the atomic spheres were applied: r(Sr1) = 1.939 Å, r(Sr2) = 2.270 Å, r(Ge1) = 1.415 Å, r(Ge2) = 1.402 Å, r(Ge3) = 1.354 Å, r(Ge4) = 1.367 Å, r(Ge5) = 1.354 Å, r(Ge6) = 1.359 Å, r(Ge7) = 1.334 Å, r(Ge8) = 1.334 Å, r(Ge9) = 1.353 Å, r(Ge10) = 1.359 Å, r(Ge11) = 1.440 Å, r(Ge12) = 1.355 Å. For the self-consistent calculation, a basis set containing Sr(5*s*,4*d*) and Ge(4*s*,4*p*) orbitals was selected with Sr(5*p*,4*f*) and Ge(4*d*) functions being downfolded. The electronic DOS was calculated using the mesh of $4 \times 12 \times 4$ *k*-points.

Analysis of the chemical bonding in positional space was performed by means of the electron localizability indicator (ELI) calculated in its ELI-D representation [20, 21] together with the electron density with a dedicated module implemented within the TB-LMTO-ASA program package. The topology of the 3D distributions of ELI-D and electron density (ED) was analyzed with the program

Table 1: Experimental details for the single-crystal X-ray diffraction measurement at room temperature (293 K) using a Rigaku AFC7 diffractometer operated with Mo$K\alpha$ radiation ($\lambda = 0.71073$ Å) and a Mercury CCD detector as well as characteristic results of the least-squares refinements.

Crystal data		
Chemical formula	$Sr(Ge_{1-x}Si_x)_6$ ($x = 0.41$)	$SrGe_6$
Space group	$P2_1/m$	$P2_1/m$
a/Å	12.284(1)	12.501(3)
b/Å	4.0377(2)	4.0628(8)
c/Å	13.050(1)	13.232(4)
β/°	103.224(4)	103.51(1)
V/Å^3	630.1(2)	653.5(5)
Calculated density/g cm^{-3}	4.35	5.32
Absorption coefficient/cm^{-1}	26.7	37.1
Data collection		
Radiation; wavelength/Å	Mo$K\alpha$; 0.71073	Mo$K\alpha$; 0.71073
Measured; unique reflections	5109; 4214	4533; 3205
$R_{equivalent}$	0.047	0.065
Reflections with $F_o > 4\,\sigma(F_o)$	1641	1709
Ranges *hkl*	$-17 \le h \le 15$	$-16 \le h \le 16$
	$-5 \le k \le 5$	$-4 \le k \le 5$
	$-18 \le l \le 17$	$-17 \le l \le 16$
R_F; R_w	0.049; 0.051	0.076; 0.079
Goodness of fit	1.02	1.04
Number of refined parameters	98	86
Residual density max; min/e^- Å^{-3}	1.3; −1.1	3.8; −2.7

CCDC 1970028 and 1970029 contain the supplementary crystallographic data for this paper. These data can be obtained free of charge from The Cambridge Crystallographic Data Centre *via* www.ccdc.cam.ac.uk/data_request/cif.

Table 2: Atomic coordinates and isotropic displacement parameters (in Å^2) of $SrGe_6$.

Atom	Wyckoff site	*x*/*a*	*y*/*b*	*z*/*c*	B_{eq} [a]
Sr1	2*e*	0.0155(3)	¼	0.2280(3)	2.4(1)
Sr2	2*e*	0.4611(4)	¼	0.7465(4)	2.8(1)
Ge1	2*e*	0.0415(4)	¼	0.4723(4)	2.7(1)
Ge2	2*e*	0.5028(3)	¼	0.4472(3)	1. 8(1)
Ge3	2*e*	0.7037(4)	¼	0.4586(3)	1.9(1)
Ge4	2*e*	0.5043(4)	¼	0.0497(4)	3.4(1)
Ge5	2*e*	0.7640(4)	¼	0.9653(3)	2.0(1)
Ge6	2*e*	0.3323(4)	¼	0.1199(3)	2.0(1)
Ge7	2*e*	0.2164(4)	¼	0.5996(3)	2.1(1)
Ge8	2*e*	0.1943(4)	¼	0.7810(3)	2.2(1)
Ge9	2*e*	0.7813(4)	¼	0.6516(3)	2.1(1)
Ge10	2*e*	0.3245(4)	¼	0.3095(3)	2.0(1)
Ge11	2e	0.9580(4)	¼	0.9490(3)	2.0(1)
Ge12	2*e*	0.7078(4)	¼	0.1343(3)	2.1(1)

[a] $B_{eq} = 1/3[B_{11}\,a^{*2}a^2 + \ldots 2B_{23}\,b^*c^*\,bc\cos\alpha]$.

DGrid [22]. Electron density and ELI-D were integrated within space regions bounded by zero-flux surfaces in the according gradient field, so-called basins, in order to obtain atomic charges (ED) and bond populations for lone-pair and bond basins (ELI-D). The latter technique follows the procedure proposed in the quantum theory of atoms in molecules (QTAIM [23]). Combined analysis of electron density and ELI-D reveals basic information for the description of the bonding situation [24, 25], in particular for intermetallic compounds [26, 27].

4 Results and discussion

After high-pressure, high-temperature synthesis of the phases $Sr(Ge_{1-x}Si_x)_6$ and $SrGe_6$, single crystalline specimens suitable for X-ray diffraction were manually isolated from crude ingots, which had been subjected to 10 GPa and 1300 K for 30 min. The thermal stability of binary $SrGe_6$ at ambient pressure is characterized by differential scanning calorimetry of a sample prepared by grinding the bulk material (Fig. 1). The onset of an effect at $T = 953$ K upon heating signalizes an exothermal decomposition of the compound. X-ray powder diffraction data of such a transformed sample (Fig. 2) revealed disintegration of $SrGe_6$ into $SrGe_2$ (modification *oP*24) and Ge (*cF*8). As these phases are stable at ambient pressure according to the phase diagram, $SrGe_6$ is a quenchable high-pressure phase, which is metastable at ambient pressure.

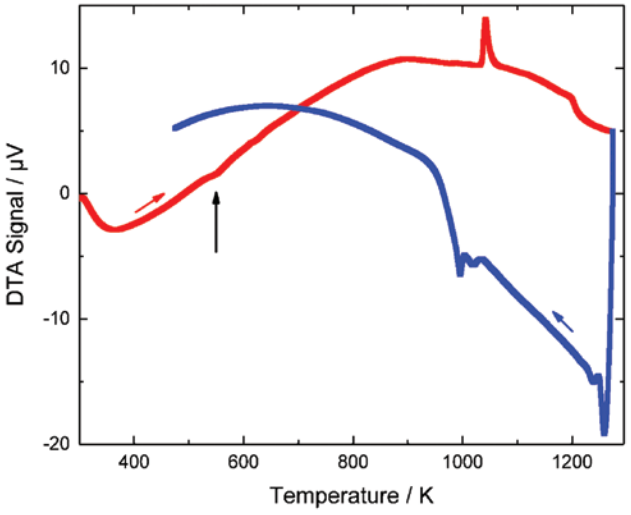

Fig. 1: Differential thermal analysis data of $SrGe_6$ at ambient pressure. With increasing temperature, the minute exothermal effect at $T = 540(10)$ K (onset temperature) evidences an exothermal, monotropic decomposition. While the nature of the second, even smaller exothermal effect at 615 K remains enigmatic, the endothermal signal at $T = 1030$ K is assigned to the melting of the eutectic mixture of $SrGe_2$ and Ge.

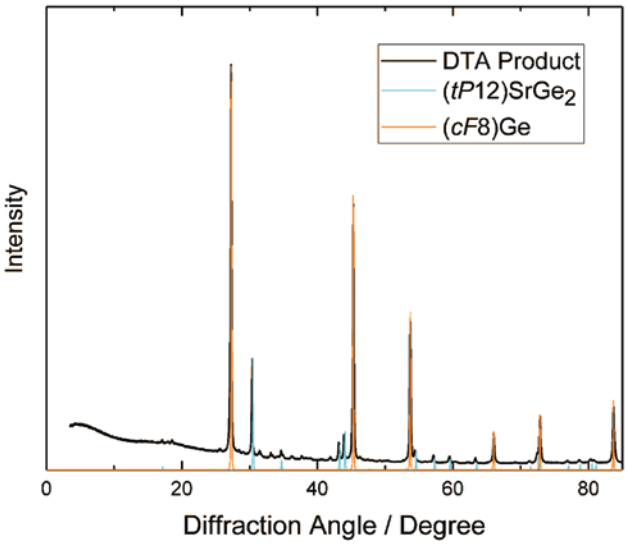

Fig. 2: Powder X-ray diffraction diagram of the decomposition products of $SrGe_6$ after heating the sample to $T = 1275$ K at ambient pressure and returning to room temperature. The disintegration of the metastable high-pressure phase mainly yields $SrGe_2$ (*oP*24 modification) and Ge (*cF*8 modification), which are the stable components at ambient pressure according to the phase diagram.

The irregular shaped single crystals for X-ray single-crystals diffraction experiments exhibits monoclinic symmetry with reflection extinctions compatible with space group $P2_1/m$ (Table 1). Structure solution was performed with charge-flip techniques as implemented in the program package WinCSD. The resulting models for $SrGe_6$ with anisotropic description of the displacement parameters converged to $R_F = 0.076$ (Tables 1–3), for $Sr(Ge_{1-x}Si_x)_6$

Table 3: Anisotropic atomic displacement parameters (Å²) for $SrGe_6$.

Atom	B_{11}	B_{22}	B_{33}	B_{13}
Sr1	2.8(2)	1.9(2)	2.7(2)	0.8(1)
Sr2	2.8(2)	2.0(2)	3.5(2)	0.7(1)
Ge1	2.8(2)	2.6(2)	2.7(2)	0.7(1)
Ge2	2.1(2)	1.7(2)	1.8(2)	0.7(1)
Ge3	2.4(2)	1.7(2)	1.8(2)	0.7(1)
Ge4	2.4(2)	4.1(3)	3.7(2)	0.9(2)
Ge5	2.5(2)	1.6(2)	2.0(2)	0.6(1)
Ge6	2.7(2)	1.5(2)	1.8(2)	0.6(1)
Ge7	2.7(2)	1.7(2)	1.9(2)	0.8(1)
Ge8	3.0(2)	1.6(2)	2.1(2)	1.0(1)
Ge9	2.4(2)	1.9(2)	2.1(2)	0.7(1)
Ge10	2.6(2)	1.6(2)	1.8(2)	0.6(1)
Ge11	2.6(2)	1.6(2)	1.8(2)	0.6(1)
Ge12	2.9(2)	1.8(2)	1.6(2)	0.7(1)

For all atoms, $B_{12} = B_{23} = 0$.

Table 4: Atomic coordinates and isotropic displacement parameters (in Å²) of $Sr(Ge_{1-x}Si_x)_6$ ($x = 0.41$).

Atom	Wyckoff site	*x*/*a*	*y*/*b*	*z*/*c*	*s.o.f.*	B_{eq} [a]
Sr1	2*e*	0.171(2)	¼	0.2283(1)	1	2.4(1)
Sr2	2*e*	0.4617(2)	¼	0.7405(2)	1	2.8(1)
Ge1/Si1	2*e*	0.0415(3)	¼	0.4740(3)	0.29(1)/0.71	2.7(1)
Ge2/Si2	2*e*	0.5031(3)	¼	0.4511(2)	0.37(1)/0.63	1.8(1)
Ge3/Si3	2*e*	0.7020(2)	¼	0.4587(2)	0.73(1)/0.27	1.9(1)
Ge4/Si4	2*e*	0.5038(3)	¼	0.0511(2)	0.41(1)/0.59	3.4(1)
Ge5/Si5	2*e*	0.7639(2)	¼	0.9651(2)	0.72(1)/0.28	2.0(1)
Ge6/Si6	2*e*	0.3304(2)	¼	0.1201(2)	0.71(1)/0.29	2.0(1)
Ge7/Si7	2*e*	0.2168(2)	¼	0.5979(2)	0.71(1)/0.29	2.1(1)
Ge8/Si8	2*e*	0.1979(2)	¼	0.7804(2)	0.65(1)/0.35	2.2(1)
Ge9/Si9	2*e*	0.7797(2)	¼	0.6514(2)	0.64(1)/0.36	2.1(1)
Ge10/Si10	2*e*	0.3278(2)	¼	0.3118(2)	0.70(1)/0.30	2.0(1)
Ge11/Si11	2e	0.9584(3)	¼	0.9500(2)	0.33(1)/0.67	2.0(1)
Ge12	2*e*	0.7071(2)	¼	0.1348(2)	0.78(1)/0.22	2.1(1)

[a] $B_{eq} = 1/3[B_{11}\, a^{*2}a^2 + \ldots 2B_{23}\, b^*c^*\, bc \cos\alpha]$.

($x = 0.41$) we obtained $R_F = 0.049$ (Tables 1 and 4–5). The results obtained by the crystal structure refinement have revealed that the phases comprise three-dimensional tetrel frameworks embedding the strontium atoms (Fig. 3). For $SrGe_6$, the Ge–Ge next-neighbor distances fall into the relatively narrow range between 2.409(4) and 2.542(4) Å in comparison to Ge–Ge distances of 2.45 Å in elemental germanium and 2.45–2.55 Å for Ba_8Ge_{43} [8, 28] and transition-metal containing Ba–Ge clathrates [29, 30]. Counting these distances as single bonds, the interpretation within the Zintl concept and the 8–*N* rule leads to an electron-precise balance of $(Sr^{2+})[(4b)Ge^0]_4[(3b)Ge^{-1})]_2$.

Table 5: Anisotropic atomic displacement parameters (in Å²) for $Sr(Ge_{1-x}Si_x)_6$ ($x = 0.41$).

Atom	B_{11}	B_{22}	B_{33}	B_{13}
Sr1	3.38(7)	2.60(5)	2.44(5)	0.44(5)
Sr2	2.67(5)	2.40(5)	2.85(6)	0.41(5)
Ge1/Si1	2.5(1)	2.29(9)	2.1(1)	0.00(8)
Ge2/Si2	2.31(9)	2.48(9)	2.18(9)	0.37(8)
Ge3/Si3	2.50(7)	2.09(6)	2.36(7)	0.46(6)
Ge4/Si4	2.33(9)	2.51(9)	2.4(1)	0.45(7)
Ge5/Si5	2.56(7)	2.22(7)	1.98(6)	0.38(6)
Ge6/Si6	2.54(7)	2.19(6)	2.13(6)	0.26(6)
Ge7/Si7	2.38(7)	2.40(7)	2.28(7)	0.26(6)
Ge8/Si8	2.62(7)	2.17(7)	2.34(7)	0.44(6)
Ge9/Si9	2.18(7)	2.44(7)	2.24(7)	0.12(6)
Ge10/Si10	2.41(7)	2.21(6)	2.21(7)	0.24(6)
Ge11/Si11	2.5(1)	2.26(9)	2.3(1)	0.60(8)
Ge12/Si12	2.66(7)	2.14(6)	2.34(7)	0.45(6)

For all atoms, $B_{12} = B_{23} = 0$.

However, the calculated electronic density of states of $SrGe_6$ reveals rather unexpectedly that the Fermi level is located above the pronounced pseudo-gap (Fig. 4). In addition, the unusual coordination of the strontium atoms (in particular Sr1) indicates atomic interactions, which significantly deviate from those observed in other germanium- and silicon-rich compounds of alkaline earth

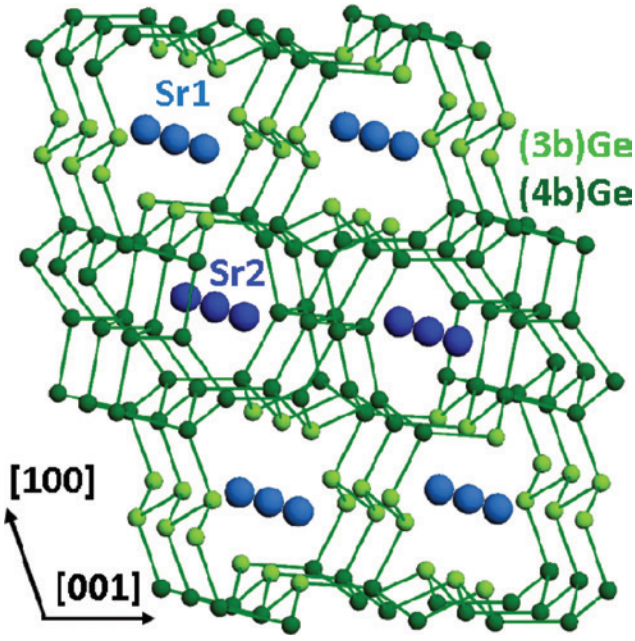

Fig. 3: Projection of the crystal structure of the isotypic phases $SrGe_6$ and $Sr(Ge_{1-x}Si_x)_6$ ($x = 0.41$). Sr1 is located in a cage formed by 15 Ge atoms and Sr2 in a polyhedron of 10 Ge atoms.

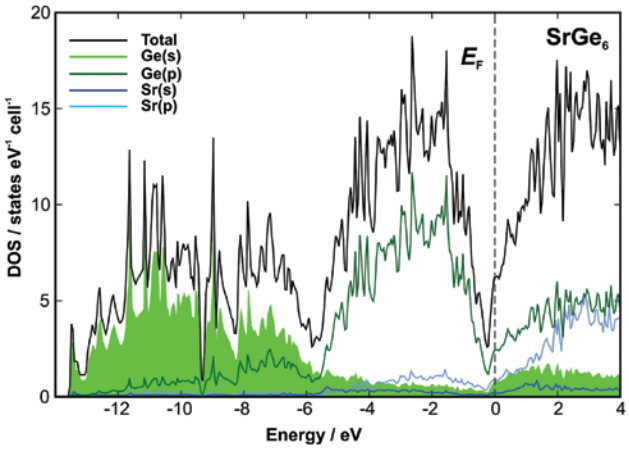

Fig. 4: Calculated total electronic density of states (DOS) together with contributions of partial states for $SrGe_6$.

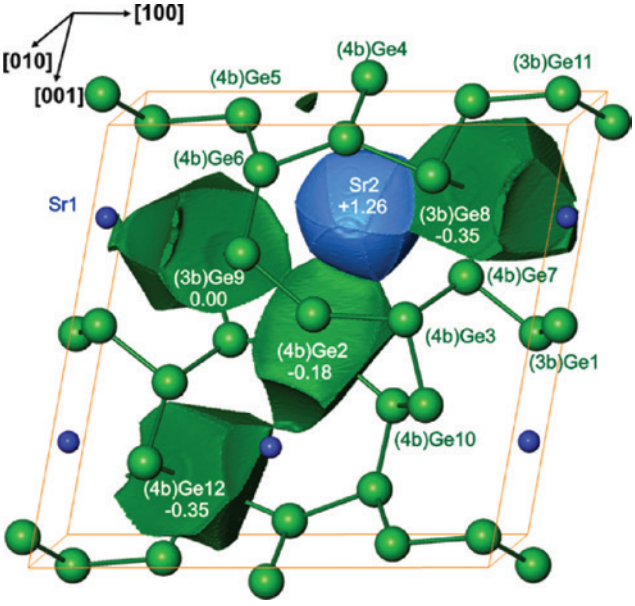

Fig. 5: The shapes of selected QTAIM atoms and their effective charges in $SrGe_6$.

metals. Thus, the organization of the (covalent) atomic interactions is studied in detail by means of bonding indicators in position space.

Analysis of the electron density using the QTAIM approach [23] is performed by integration of the electron density within basins. From the resulting values, the respective atomic number is subtracted for yielding effective charges. Although the strontium atoms have markedly different coordination spheres (a more convex polyhedron of 10 Ge for Sr2 and 15 Ge ligands in concave coordination for Sr1), the results reveal that the strontium atoms have shapes, which are close to spherical symmetry and indicate ionic character (Fig. 5). Despite the different coordination, both strontium atoms have practically equal effective QTAIM charges of +1.23 and +1.26 for Sr1 and Sr2, respectively. These values are in good agreement with values between 1.20 and 1.54 obtained for other intermetallic compounds of strontium [11, 31–33]. The shapes of the germanium atoms have polyhedral character with flat contact faces between neighboring atoms, which is characteristic for non-polar covalent bonding.

The calculated charge transfers from the strontium to the germanium atoms (Fig. 5) are quite small or even close to zero (from −0.35 to +0.09), which is attributed to the small Sr:Ge ratio in the compound. The extremely small charge of Ge5 correlates with its special environment as only germanium atoms are located in its coordination sphere; the shortest distance Ge5–Sr1 amounts to 4.107(6) Å and is, thus, well outside the range of 3.17–3.62 Å for the other Ge atoms. The rather unexpected charges for (3b) Ge1 and (3b)Ge9 do not correlate with their homo-atomic coordination, as the charges for the other three-bonded atoms Ge8 and Ge11 are negative. The first coordination sphere of the atoms Ge2–Ge7, Ge10 and Ge12 consist of germanium atoms only; the other four (Ge1, Ge8, Ge9 and Ge11) have three germanium and one strontium neighbors each.

In order to understand the role of the three- and four-bonded germanium atoms in the Sr–Ge interactions, further analysis of chemical bonding in $SrGe_6$ was performed by applying the electron localizability indicator (ELI) approach (Fig. 6). The ELI-D distribution in the penultimate shell of the strontium atoms shows deviations from spherical symmetry (structuring [24]). The ELI-D structuring in the penultimate shell is a fingerprint of the participation of these electrons in interactions within the valence region [24, 34]. Quantitative characterization of this trend using the so-called structuring index ε (the difference between the maximal ELI-D value in the shell and the value at which the isosurface of the shell closes [24]) reveals a difference between Sr1 ($\varepsilon = 0.06$) and Sr2 ($\varepsilon = 0.02$). These values are smaller than those recently found for $BaSi_3$ ($\varepsilon = 0.04–0.07$) [35], characterizing the reduced need for the inner electrons for the bonding in $SrGe_6$ in comparison to the Ba-Si interactions in $BaSi_3$ with smaller tetrel ratio. This trend is in agreement with that recently observed for binary yttrium gallium compounds, in which ε changes from 0.024 via 0.030 to 0.064–0.079 for YGa_6, YGa and *t*-Y_5Ga_3, respectively [36].

In the valence region, only two different kinds of ELI-D maxima are observed. The attractors of the first type are located close to the Ge–Ge contacts, revealing covalent homoatomic bonding. The shift of the maxima positions from the Ge–Ge lines toward the neighboring Sr atoms

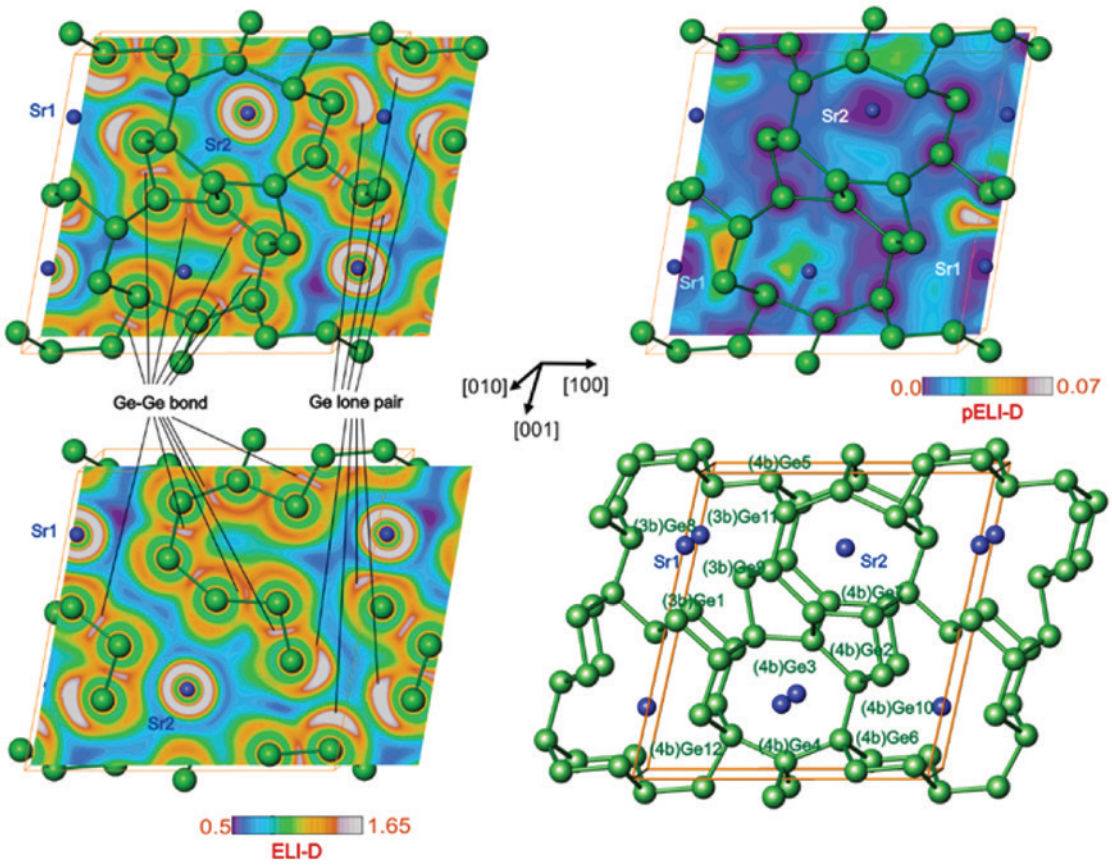

Fig. 6: Electron localizability indicator and atomic interactions in $SrGe_6$: (top left) distribution of ELI-D in the plane at $y = 0.25$; (bottom left) distribution of ELI-D in the plane at $y = 0.75$ visualizing the Ge–Ge bonds and lone pairs on three-bonded germanium atoms; (top right) distribution of partial ELI-D in the plane at $y = 0.25$ revealing the interactions within the large cages around the strontium atoms (bottom right) bonding picture as obtained from quantum-mechanical bonding analysis.

indicates additional polar interactions between the Ge framework and the strontium atoms (Fig. 6, left, top and bottom). The integration of the electron density within the bonding basins yields populations for the Ge–Ge bonds between 1.85 and 2.25 electrons, which corresponds in good approximation to two-center two-electron covalent bonds. The attractors of the second type are located on the 'outer' side of the three-bonded Ge atoms (Ge1, Ge8, Ge9 and Ge11) and visualize another type of interaction. Their basin populations show larger values (2.06–2.52 electrons) as often observed for this type of attractor. In a Sr-free framework, the basins defined by zero-flux surfaces in the gradient field of ELI-D would have contact with the core basins of the germanium atoms, i.e. they reflect the presence of a lone pair. In $SrGe_6$, these 'lone-pairs' indicate a polar (multi-atomic) bonding between the anionic and cationic parts of the crystal structure.

While in the coordination sphere of Sr2 only homoatomic (4b)Ge–(4b)Ge bonds are present, all three-bonded germanium atoms contribute with their 'lone-pairs' to the coordination sphere of Sr1. The interaction between Ge1 and Sr1 is even dominantly two-atomic. Such a feature has not been observed earlier in intermetallic (anionic) cage compounds. The 'lone pairs' of Ge8, Ge9 and Ge11 reflect multi-atomic bonding which stabilizes the 'neck' in the framework. This feature distinguishes $SrGe_6$ from typical cage compounds like type-I clathrates of barium, in which the 'necks' between the cavities are stabilized by direct bonds between the framework atoms [30, 37].

In general, the results of the topological analysis of electron density and electron localizability indicator in $SrGe_6$ are in agreement with the Zintl-like bonding picture (Fig. 6, right, bottom). The ELI-D distribution reveals characteristic topological features for three- and four-bonded germanium atoms. The convex character of the coordination polyhedron for Sr2 is a consequence of the covalent Ge–Ge bonds on the surface of the polyhedron. The cation coordination is similar to that of other germanium- and

silicon-rich compounds of the alkaline earth metals (MSi_6 [1–3], $SrGe_{6-x}$ [13], and the clathrates of Ba and Sr with Si or Ge [8, 28]). The partially concave shape of the coordination polyhedron of Sr1 is due to the lone pairs located at the three-bonded germanium atoms.

Despite the electron-precise charge balance, the Fermi level is positioned slightly above the pseudo-gap in the electronic density of states (DOS), where it would be expected for a Zintl-like bonding picture (Fig. 4). Such a distribution of the DOS is characteristic for compounds with so-called excess electrons, i.e. electrons, which are not necessary for the formation of two-center two-electron bonds within the Zintl anion. In order to clarify in which part of the crystal structure of $SrGe_6$ these electrons contribute to the atomic interactions, the partial ELI-D (pELI-D) approach was employed. The pELI-D was calculated for states being located between the drop (−0.23 eV) and the Fermi level [24] (Fig. 6, right, top). The results provide evidence that the excess electrons contribute to interactions between the filler cation and the framework. Similar situations have been observed for $MgSi_5$ [38] or the new clathrate Sr_8Si_{46} [39]. In $SrGe_6$, the excess electrons are participating in the bonding around Sr1 with the largest contribution to the two-atomic Sr–Ge1 bond as already detected by the analysis of ELD-D (see above). Smaller contributions are observed for the coordination sphere of Sr2. The pEDI-D distribution here is similar to the picture found recently for Sr_8Si_{46}. Because only the last feature reflects an additional attractive interaction in the crystal structure, one may assume that a defect of strontium in the crystal structure would lower the Fermi level towards the middle of the dip.

5 Summary

The new high-pressure phase $SrGe_6$ comprises a framework which is built from three- and four-bonded germanium atoms. Thus, the resulting electron count is in accordance with the 8–N rule, $(Sr^{2+})[(4b)Ge^0]_4[(3b)Ge^{-1})]_2$, whereas earlier studied hexasilicides MSi_6 (M = Ca, Sr, Ba; Eu) are typical electron-excess compounds with covalent networks of four-bonded silicon atoms and a surplus of two electrons, $(M^{2+}[(4b)Si^0]_6 \times 2e^-)$ [1–5]. Although the electron balance of $SrGe_6$ (and $Sr(Ge_{1-x}Si_x)_6$; $x = 0.41$) would be compatible with the Zintl concept, the calculated electronic structure of $SrGe_6$ indicates a more complex bonding situation than that of typical semiconducting or insulating compounds. The Fermi level of $SrGe_6$ is located above a weakly developed pseudo-gap and the Zintl-like organization of electron transfer and framework bonds is supplemented by additional Sr–Ge interactions in the concave coordination polyhedra of strontium atoms.

Acknowledgements: We thank Susann Leipe for high-pressure syntheses, Marcus Schmidt and Susann Scharsach for DTA characterizations as well as Ulrich Burkhardt, Monika Eckert and Sylvia Kostmann for metallographic investigations.

References

[1] A. Wosylus, Yu. Prots, U. Burkhardt, W. Schnelle, U. Schwarz, *Sci. Technol. Adv. Mater.* **2007**, *8*, 383.
[2] A. Wosylus, Yu. Prots, U. Burkhardt, W. Schnelle, U. Schwarz, Yu. Grin, *Z. Naturforsch.* **2006**, *61b*, 1485.
[3] A. Wosylus, Yu. Prots, U. Burkhardt, W. Schnelle, U. Schwarz, Yu. Grin, *Solid State Sci.* **2006**, *8*, 773.
[4] S. Yamanaka, S. Maekawa, *Z. Naturforsch.* **2006**, *61b*, 1493.
[5] A. Wosylus, R. Demchyna, Yu. Prots, W. Schnelle, U. Schwarz, *Z. Kristallogr. NCS* **2009**, *224*, 347.
[6] B. Eisenmann, H. Schäfer, R. Zahler, *J. Less-Common Met.* **1986**, *118*, 43.
[7] H. Fukuoka, S. Yamanaka, E. Matsuoka, T. Takabatake, *Inorg. Chem.* **2005**, *44*, 1460.
[8] W. Carrillo-Cabrera, S. Budnyk, Yu. Prots, Yu. Grin, *Z. Anorg. Allg. Chem.* **2004**, *630*, 2267.
[9] A. Kaltzoglou, T. F. Fässler, M. Christensen, S. Johnsen, B. B. Iversen, I. A. Presniakov, A. N. Sobolev, A. V. Shevel'kov, *J. Mater. Chem.* **2008**, *18*, 5630.
[10] T. Leisegang, D. C. Meyer, T. Doert, G. Zahn, T. Weißbach, D. Souptel, G. Behr, P. Paufler. *Z. Kristallogr.* **2005**, *220*, 128.
[11] J. D. Bryan, G. D. Stucky, *Chem. Mater.* **2001**, *13*, 253.
[12] W. Carrillo-Cabrera, S. Paschen, Yu. Grin, *J. Alloys Compd.* **2002**, *333*, 4.
[13] U. Schwarz, R. Castillo, A. Wosylus, L. Akselrud, Y. Prots, B. Wahl, Th. Doert, M. Bobnar, Yu. Grin, *Z. Naturforsch.* **2019**, *74b*, 137.
[14] D. Walker, M. A. Carpenter, C. M. Hitch, *Am. Mineral.* **1990**, *75*, 1020.
[15] D. A. Young, *Phase Diagrams of the Elements*, UC Press, Oxford, **1991**, p. 122 and references therein.
[16] L. Akselrud, Yu. Grin, *J. Appl. Cystallogr.* **2014**, *47*, 803.
[17] O. Jepsen, O. K. Andersen, TB-LMTO-ASA (version 47), Max-Planck-Institut für Festkörperforschung, Stuttgart (Germany) **2000**.
[18] U. von Barth, L. Hedin, *J. Phys.* **1972**, *C5*, 1629.
[19] O. K. Andersen, *Phys. Rev.* **1975**, *B12*, 3060.
[20] M. Kohout, *Int. J. Quantum Chem.* **2004**, *97*, 651.
[21] M. Kohout, *Faraday Discuss.* **2007**, *135*, 43.
[22] M. Kohout, DGrid (versions 4.6–5.0), Radebeul (Germany) **2018**.
[23] R. F. W. Bader, *Atoms in molecules: A Quantum Theory*, Oxford University Press, Oxford, **1999**.
[24] F. R. Wagner, V. Bezugly, M. Kohout, Yu. Grin, *Chem. Eur. J.* **2007**, *13*, 5724.

[25] M. Kohout, A. Savin, *Int. J. Quantum Chem.* **1996**, *60*, 875.
[26] Yu. Grin, in *Comprehensive Inorganic Chemistry II: From Elements to Applications*, (2nd edition), Vol. 2, (series Eds.: J. Reedijk, K. R. Poeppelmeier), *Transition Elements, Lanthanides and Actinides*, (Eds.: E. V. Antipov, A. M. Abakumov, A. V. Shevelkov), Elsevier, Amsterdam, **2013**, pp. 359–373.
[27] D. Bende, F. R. Wagner, Yu. Grin, *Inorg. Chem.* **2015**, *54*, 3970.
[28] W. Carrillo-Cabrera, J. Curda, K. Peters, S. Paschen, M. Baenitz, Yu. Grin, H. G. von Schnering, *Z. Kristallogr. NCS* **2000**, *215*, 321.
[29] H. Zhang, H. Borrmann, N. Oeschler, C. Candolfi, W. Schnelle, M. Schmidt, U. Burkhardt, M. Baitinger, J.-T. Zhao, Yu. Grin, *Inorg. Chem.* **2011**, *50*, 1250.
[30] P.-F. Lory, S. Pailhès, V. M. Giordano, H. Euchner, H. D. Nguyen, R. Ramlau, H. Borrmann, M. Schmidt, M. Baitinger, M. Ikeda, P. Tomeš, M. Mihalkovi, C. Allio, M. R. Johnson, H. Schober, Y. Sidis, F. Bourdarot, L. P. Regnault, J. Ollivier, S. Paschen, Yu. Grin, M. de Boissieu, *Nat. Commun.* **2017**, *8*, 1.
[31] R. Castillo, W. Schnelle, A. I. Baranov, U. Burkhardt, M. Bobnar, R. Cardoso-Gil, U. Schwarz, Yu. Grin, *Z. Naturforsch. B* **2016**, *71*, 585.
[32] X.-J. Feng, Y. Prots, M. Bobnar, M. P. Schmidt, W. Schnelle, J.-T. Zhao, Yu. Grin, *Chem. Eur. J.* **2015**, *21*, 14471.
[33] A. Palasyuk, Yu. Grin, G. J. Miller, *J. Am. Chem. Soc.* **2014**, *136*, 3108.
[34] M. Kohout, F. R. Wagner, Yu. Grin, *Theor. Chem. Acc.* **2002**, *108*, 150.
[35] J.-M. Hübner, L. Akselrud, W. Schnelle, U. Burkhardt, M. Bobnar, Yu. Prots, Yuri Grin, U. Schwarz, *Materials* **2019**, *12*, 145.
[36] Yu. Grin, A. Fedorchuk, R. J. Faria, F. R. Wagner, *Crystals* **2018**, *8*, 99.
[37] R. Castillo, W. Schnelle, M. Bobnar, U. Burkhardt, B. Böhme, M. Baitinger, U. Schwarz, Yu. Grin, *Z. Anorg. Allg. Chem.* **2015**, *641*, 206.
[38] J.-M. Hübner, W. Carrillo-Cabrera, Yu. Prots, M. Bobnar, U. Schwarz, Yuri Grin, *Angew. Chem. Int. Ed.* **2019**, *58*, 12914.
[39] J.-M. Hübner, Yu. Prots, W. Schnelle, M. Bobnar, M. König, M. Baitinger, P. Simon, W. Carrillo-Cabrera, A. Ormeci, E. Svanidze, Yu. Grin, U. Schwarz, *Chem. Eur. J.* DOI: 10.1002/chem.201904170.